# Fully automated Segmentation using Distance Regularized Level Set and Deep-structured Learning and Inference

Tuan Anh Ngo and Gustavo Carneiro

**Abstract** We introduce a new segmentation methodology that combines the structured output inference from deep belief networks and the delineation from level set methods to produce accurate segmentation of anatomies from medical images. Deep belief networks can be used in the implementation of accurate segmentation models if large annotated training sets are available, but the limited availability of such large datasets in medical image analysis problems motivates the development of methods that can circumvent this demand. In this chapter, we propose the use of level set methods containing several shape and appearance terms, where one of the terms consists of the result from the deep belief network. This combination reduces the demand for large annotated training sets from the deep belief network and at the same time increases the capacity of the level set method to model more effectively the shape and appearance of the visual object of interest. We test our methodology on the Medical Image Computing and Computer Assisted Intervention (MICCAI) 2009 left ventricle segmentation challenge dataset and on Japanese Society of Radiological Technology (JSRT) lung segmentation dataset, where our approach achieves the most accurate results of the field using the semi-automated methodology and state-of-the-art results for the fully automated challenge.

Tuan Anh Ngo
Department of Computer Science Faculty of Information Technology, Vietnam National University of Agriculture, Vietnam e-mail: ntanh@vnua.edu.vn

Gustavo Carneiro
Australian Centre for Visual Technologies, The University of Adelaide, Australia e-mail: gustavo.carneiro@adelaide.edu.au

This work is an extension of the papers published by the same authors at the IEEE Conference on Computer Vision and Pattern Recognition (CVPR 2014) [1] and the IEEE International Conference on Image Processing (ICIP 2015) [2].

## 1 Introduction

The segmentation of anatomies from medical images is an important stage in the process of analysing the health of a particular organ. For instance, the segmentation of the endocardium and epicardium from the left ventricle (LV) of the heart using cardiac cine Magnetic Resonance (MR) [3, 4], as shown in Fig. 1-(a), is necessary for the assessment of the cardiovascular system function and structure. The main challenges in the LV segmentation from MR are related to the need to process the various slices from the short axis view, where the area of the LV changes considerably, and to be robust to trabeculations and papillary muscles. Another example is the segmentation of the lung from digital chest X-ray (CXR) [5], as displayed in Fig. 1-(b), which is needed for computing lung volume or estimating shape irregularities [6] for screening and detecting pulmonary pathologies. The lung segmentation problem is challenging due to the large shape and appearance variations of the lung, and the presence clavicle bones and rib cage. One of the main challenges involved in these medical image analysis segmentation problems is that the usefulness of a system is related to the accuracy of its segmentation results, which is usually correlated to the size of the annotated training set available to build the segmentation model. However, large annotated training sets are rarely available for medical image analysis segmentation problems, so it is important to develop methods that can circumvent this demand.

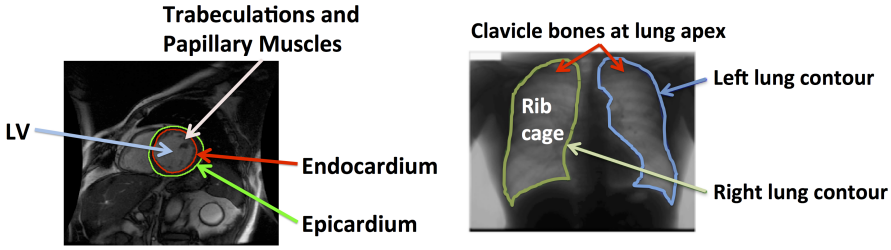


(a) Left ventricle segmentation from MR (b) Lung segmentation from CXR

**Fig. 1** LV segmentation from cardiac cine MR imaging [4] (a), and lung segmentation from digital chest X-ray [5] (b).

Currently the main approaches explored in medical image segmentation problems are the following: active contour models, machine learning models, and hybrid active contour and machine learning models. One of most successful methodologies explored in the field is the active contour models [7, 8] that is generally represented by an optimisation that minimises an energy functional which varies the shape of a contour using internal and external hand-crafted constraints. Internal constraints are represented by terms that associate cost with contour bending, stretching or shrinking, and the external constraints use the image data to move the contour towards (or away from) certain features, such as edges. These constraints usually rely on shape

or appearance models that require small training sets. The main challenges faced by active contour models are their inability to model robustly the shape and appearance variations presented by the visual object of interest.

Machine learning methods allow a more robust modelling of the shape and appearance of visual objects [9, 10], which generally translates into more accurate segmentation results. However, the challenges presented in medical image applications in terms of segmentation accuracy requirements and large shape and appearance variations of the visual object of interest imply that the models must have high capacity, requiring a large and rich annotated training set. This means that the acquisition of comprehensive annotated training sets is one of the main foci in the design of machine learning models, which is a complicated task, particularly in medical image analysis. More recent machine learning methodologies are based on models with less capacity, which reduces the need for large and rich training sets, where the idea lies in the combination of active contour models and Markov random fields (MRF) [11, 12, 13]. However, the main issues of these approaches is that MRF models present large memory complexity, which limits the size of the input image (or volume) to be segmented.

We propose a new methodology that combines an active contour model (distance regularised level sets) [14] with a machine learning approach (deep belief network) [15]. Deep belief networks (DBN) are represented by a high capacity model that needs large amounts of training data to be robust to the appearance and shape variations of the object of interest, but the two-stage training (consisting of a pre-training based on a large un-annotated training set, followed by a fine-tuning that relies on a relatively small annotated training set) [15] reduces the need for annotated training images. Nevertheless, medical image analysis datasets are generally too small to produce robust DBN models, so its use as a shape term in a level set method can compensate for its lack of robustness and at the same time can improve the accuracy of the level set method. In addition, this combination does not present the the large memory complexity faced by MRF models. We show the effectiveness of our approach on two distinct datasets: the Medical Image Computing and Computer Assisted Intervention (MICCAI) 2009 LV segmentation challenge dataset [4] and the Japanese Society of Radiological Technology (JSRT) lung segmentation dataset [16]. Our experiments show that our approach produces the best result in the field when we rely on a semi-automated segmentation (i.e., with manual initialisation) for both datasets. Also, our fully automated approach produces a result that is on par with the current state of the art on the MICCAI 2009 LV segmentation challenge dataset.

## 2 Literature Review

The proposed segmentation methodology can be used in various medical image analysis problems, but we focus on two applications that are introduced in this section. The first application is the segmentation of the endocardial and epicardial

borders of the LV from short axis cine MR images, and the second application is the lung segmentation from CXR images. The LV segmentation (see Fig. 1-(a)) is challenging due to the lack of gray level homogeneity in the imaging of the LV, which happens because of blood flow, papillary muscles and trabeculations, and the low resolution of the apical and basal images [3]. It is possible to to categorise LV segmentation approaches with three properties: 1) segmentation method (region and edge based, pixel classification, deformable models, active appearance and shape models), 2) prior information (none, weak, and strong), and 3) automated localisation of the heart (time-based or object detection). According to Petitjean et al.'s analysis [3] of the MICCAI 2009 challenge results [4], the highest accuracy is obtained from image-based methodologies [17, 18] based on thresholding or dynamic programming applied to image segmentation results. However, these methods usually require user interaction and show difficulties in segmenting the LV in all cardiac phases. These drawbacks have been addressed by more sophisticated methods [19, 20, 21], but their segmentation accuracy is not as high as the simpler image-based methods above. Moreover, the use of techniques specific to the LV segmentation problem [17, 18, 22] produces more accurate results when compared to more general approaches [19, 23]. The main conclusion reached by Petitjean et al.[3] is that Jolly's methodology [21] is the most effective because it is fully automatic and offers the best compromise between accuracy and generalisation. The most effective methodology in the MICCAI 2009 challenge for the semi-automated case (i.e., that requires a user input in terms of the initialisation for the segmentation contour) has been developed by Huang et al. [18].

The challenges in the lung segmentation problem (see Fig. 1-(b)) are related to the presence of strong edges at the rib cage and clavicle, the lack of a consistent lung shape among different cases, and the appearance of the lung apex. Current techniques are based on methods that combine several methodologies, such as landmark learning and active shape and appearance models [24, 25] or MRF and non-rigid registration [5]. Although presenting state-of-the-art segmentation results, these methods show some drawbacks: landmark learning is a hard problem that is based on hand-crafted feature detector and extractor, active shape and appearance models make strong assumptions about the distribution of landmarks, and MRF inference has high memory complexity that limits the input image size.

Finally, it is important to note that image segmentation can be posed as a structured output learning and inference problem [26], where the classification is represented by a multi-dimensional binary vector. Traditionally, structured output models use a large margin learning formulation [27], but a natural way to represent a structured learning is with a multi-layer perceptron, where the output layer consists of a multi-dimensional binary vector denoting the segmentation [28]. The recent renaissance of deep learning methods originated from the development of an efficient learning algorithm for training DBN [15], which allowed the development of structured inference and learning with DBN [29, 30, 31, 32]. Similarly, the method proposed by Farabet et al. [30] parses a scene into several visual classes using convolutional neural networks. Nevertheless, the papers above show that DBNs can work

solidly in structured output problems only with the availability of large annotated training sets that allows the modelling of a robust DBN.

## 3 Methodology

In order to explain the segmentation algorithm, let us assume that we have an annotated dataset (Fig. 2), represented by $\mathscr{D} = \{(\mathbf{v}, \mathbf{c}, \mathbf{y})_i\}_{i=1}^{|\mathscr{D}|}$, where $\mathbf{v} : \Omega \rightarrow \mathbb{R}$ represents an image of the visual object of interest (with $\Omega \subseteq \mathbb{R}^2$ denoting the image lattice), $\mathbf{c} : [0,1] \rightarrow \Omega$ denotes the explicit contour representation of the segmentation, and the binary segmentation map is represented by $\mathbf{y} : \Omega \rightarrow \{0,1\}$, where 1 represents the foreground (i.e., points inside the contour $\mathbf{c}$) and 0 denotes the background (i.e., points outside the contour $\mathbf{c}$). Below, we first explain the segmentation method based on the distance regularised level set (DRLS), then we describe the DBN model and the shape prior.

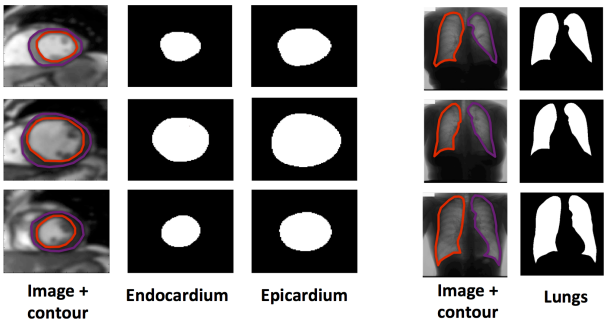


(a) Left ventricle images and annotation (b) Lung images and annotation

**Fig. 2** Left ventricle images $\mathbf{v}$ with overlaid endocardial and epicardial segmentation contours $\mathbf{c}$ and respective segmentation maps $\mathbf{y}$ in (a), and lung images with overlaid left and right segmentation contours and respective segmentation maps in (b).

The main segmentation algorithm is based on the distance regularised level set (DRLS) method [14], where the energy functional is represented by:

$$\mathscr{E}(\phi, \phi_{\text{DBN}}, \phi_{\text{PRIOR}}) = \mu \mathscr{R}_p(\phi) + \mathscr{E}_{\text{ext}}(\phi, \phi_{\text{DBN}}, \phi_{\text{PRIOR}}), \tag{1}$$

where $\phi : \Omega \rightarrow \mathbb{R}$ represents the signed distance function, defined by

$$\phi(\mathbf{x}) = \begin{cases} -d(\mathbf{x}, \Omega^{out}), & \text{if } \mathbf{x} \in \Omega^{in} \\ +d(\mathbf{x}, \Omega^{in}), & \text{if } \mathbf{x} \in \Omega^{out} \end{cases}, \tag{2}$$

where $\Omega^{in} = \{\mathbf{x} \in \Omega | \mathbf{y}(\mathbf{x}) = 1\}$, $\Omega^{out} = \{\mathbf{x} \in \Omega | \mathbf{y}(\mathbf{x}) = 0\}$, and $d(\mathbf{x}, \Omega) = \inf_{\mathbf{z} \in \Omega} \|\mathbf{x} - \mathbf{z}\|_2$, assuming that $\mathbf{y}$ denotes the segmentation map. Also in (1), the distance regularisation $\mathscr{R}_p(\phi) = \int_\Omega 0.5(|\nabla\phi(\mathbf{x})| - 1)^2 d\mathbf{x}$ guarantees that $|\nabla\phi(\mathbf{x})| \approx 1$, which avoids the re-initialisations during the segmentation process [14] (a common issue in level set methods), and

$$\mathscr{E}_{\text{ext}}(\phi, \phi_{\text{DBN}}, \phi_{\text{PRIOR}}) = \lambda\mathscr{L}(\phi) + \alpha\mathscr{A}(\phi) + \beta\mathscr{S}(\phi, \phi_{\text{DBN}}) + \gamma\mathscr{S}(\phi, \phi_{\text{PRIOR}}), \quad (3)$$

with the length term $\mathscr{L}(\phi) = \int_\Omega g\delta(\phi(\mathbf{x}))|\nabla\phi(\mathbf{x})|d\mathbf{x}$ (with $\delta(.)$ denoting the Dirac delta function and $g \triangleq \frac{1}{1+|\nabla G_\sigma * I|}$ representing the edge indicator function), the area $\mathscr{A}(\phi) = \int_\Omega gH(-\phi(\mathbf{x}))d\mathbf{x}$ (with $H(.)$ denoting the Heaviside step function), and $\mathscr{S}(\phi, \phi_\kappa) = \int_\Omega (\phi(\mathbf{x}) - \phi_\kappa(\mathbf{x}))^2 d\mathbf{x}$ (with $\kappa \in \{\text{DBN, PRIOR}\}$) representing the shape term [33] that drives $\phi$ either towards the shape $\phi_{\text{DBN}}$, which is the distance function inferred from the deep belief network (DBN) structured inference described below, or the shape prior $\phi_{\text{PRIOR}}$, estimated from the training set and also described in more detail below. The gradient flow of the energy $\mathscr{E}(\phi)$ is then defined as follows:

$$\begin{aligned}\frac{\partial\phi}{\partial t} =& \mu\,\text{div}(d_p(|\nabla\phi|)\nabla\phi) + \lambda\delta(\phi)\text{div}(g\frac{\nabla\phi}{|\nabla\phi|}) + \alpha g\delta(\phi) + \\ & 2\beta(\phi(\mathbf{x}) - \phi_{\text{DBN}}(\mathbf{x})) + 2\gamma(\phi(\mathbf{x}) - \phi_{\text{PRIOR}}(\mathbf{x})),\end{aligned} \quad (4)$$

where $\text{div}(.)$ denotes the divergence operator, and $d_p(.)$ denotes the derivative of the function $p(.)$ defined in (1).

The segmentation is obtained from the minimisation of the energy functional in (1) from the steady solution of the gradient flow equation [14] $\frac{\partial\phi}{\partial t} = -\frac{\partial\mathscr{E}}{\partial\phi}$, where $\partial\mathscr{E}/\partial\phi$ is the Gâteaux derivative of the functional $\mathscr{E}(\phi)$ and $\frac{\partial\phi}{\partial t}$ is defined in (4). The main idea of the DRLS [14] is then to iteratively follow the steepest descent direction (4) until convergence, resulting in the final steady solution.

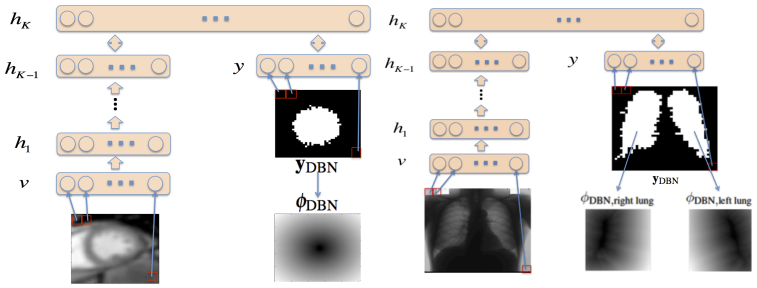


(a) Left ventricle DBN (b) Lungs DBN

**Fig. 3** Deep belief network that produces the segmentation maps $\mathbf{y}_{\text{DBN}}$ and respective signed distance function $\phi_{\text{DBN}}$ for the left ventricle structures (epicardium and endocardium) in (a) and left and right lungs in (b).

The structured inference from the DBN (Fig. 3) produces the following segmentation map:

$$\mathbf{y}_{\text{DBN}} = \arg\max_{\mathbf{y}} \sum_{\mathbf{h}_1} .. \sum_{\mathbf{h}_K} P(\mathbf{v}, \mathbf{h}_1, ..., \mathbf{h}_K, \mathbf{y}; \Theta), \tag{5}$$

where $\mathbf{v}$ represents the input image, $\mathbf{h}_k \in \{0,1\}^{|\mathbf{h}_k|}$ represents the $|\mathbf{h}_k|$ hidden nodes of layer $k \in \{1,..,K\}$ of the deep belief network, and $\Theta$ denotes the DBN parameters (weights and biases). The probability term in (5) is computed as

$$P(\mathbf{v}, \mathbf{h}_1, ..., \mathbf{h}_K, \mathbf{y}) = P(\mathbf{h}_K, \mathbf{h}_{K-1}, \mathbf{y}) \left( \prod_{k=1}^{K-2} P(\mathbf{h}_{k+1} | \mathbf{h}_k) \right) P(\mathbf{h}_1 | \mathbf{v}), \tag{6}$$

where $-\log P(\mathbf{h}_K, \mathbf{h}_{K-1}, \mathbf{y}) \propto \mathscr{E}_{\text{RBM}}(\mathbf{h}_K, \mathbf{h}_{K-1}, \mathbf{y})$ with

$$\mathscr{E}_{\text{RBM}}(\mathbf{h}_K, \mathbf{h}_{K-1}, \mathbf{y}) = -\mathbf{b}_K^\top \mathbf{h}_K - \mathbf{a}_{K-1}^\top \mathbf{h}_{K-1} - \mathbf{a}_y^\top \mathbf{y} - (\mathbf{h}_K)^\top \mathbf{W}_K \mathbf{h}_{K-1} - (\mathbf{h}_K)^\top \mathbf{W}_y \mathbf{y} \tag{7}$$

representing the energy function of a restricted Boltzmann machine (RBM) [15], where $\mathbf{b}_K, \mathbf{a}_{K-1}, \mathbf{a}_y$ denote the bias vectors and $\mathbf{W}_K, \mathbf{W}_y$ are the weight matrices. Also in (6), we have

$$P(\mathbf{h}_{k+1} | \mathbf{h}_k) = \prod_j P(\mathbf{h}_{k+1}(j) = 1 | \mathbf{h}_k), \tag{8}$$

with $P(\mathbf{h}_{k+1}(j) = 1 | \mathbf{h}_k) = \sigma(\mathbf{b}_{k+1}(j) + \mathbf{h}_k^\top \mathbf{W}_{k+1}(:, j))$, $P(\mathbf{h}_1(j) = 1 | \mathbf{v}_{\mathbf{m}_\phi}) = \sigma(\mathbf{b}_1(j) + \frac{\mathbf{v}_{\mathbf{m}_\phi}^\top \mathbf{W}_1(:,j)}{\sigma^2})$ (we assume zero-mean Gaussian visible units for the DBN), where $\sigma(x) = \frac{1}{1+e^{-x}}$, the operator $(j)$ returns the $j^{th}$ vector value, and $(:, j)$ returns the $j^{th}$ matrix column. The signed distance function $\phi_{\text{DBN}}$ is then computed with (2). The DBN in (5) is trained in two stages. The first stage is based on the unsupervised bottom-up training of each pair of layers, where the weights and biases of the network are learned to build an auto-encoder for the values at the bottom layer, and the second stage is based on a supervised training that uses the segmentation map $\mathbf{y}$ as the training label [15]. The structured inference process consists of taking the input image and performing bottom-up inferences, until reaching the top two layers, which form an RBM, and then initialise the layer $\mathbf{y} = \mathbf{0}$ and perform Gibbs sampling on the layers $\mathbf{h}_K$, $\mathbf{h}_{K-1}$ and $\mathbf{y}$ until convergence [15]. The signed distance function $\phi_{\text{DBN}}$ is then computed with (2) from $\mathbf{y}_{\text{DBN}}$.

The shape prior (Fig. 4) is computed with the mean of the manual annotations $\{\mathbf{y}_i\}_{i \in \mathscr{T}}$, where $\mathscr{T} \subset \mathscr{D}$ denotes the training set, as follows: $\bar{\mathbf{y}}(\mathbf{x}) = \frac{1}{|\mathscr{T}|} \sum_{i=1}^{|\mathscr{T}|} \mathbf{y}_i(\mathbf{x})$, where $\mathbf{x} \in \Omega$. Assuming that each element of the mean map $\bar{\mathbf{y}}$ is between 0 and 1, the shape prior is computed as

$$\mathbf{y}_{\text{PRIOR}}(\mathbf{x}) = \begin{cases} 1, \text{ if } \bar{\mathbf{y}}(\mathbf{x}) > 0.5 \\ 0, \text{ if } \bar{\mathbf{y}}(\mathbf{x}) \leq 0.5 \end{cases}. \tag{9}$$

The signed distance function $\phi_{\text{PRIOR}}$ is then computed with (2) from $\mathbf{y}_{\text{PRIOR}}$.

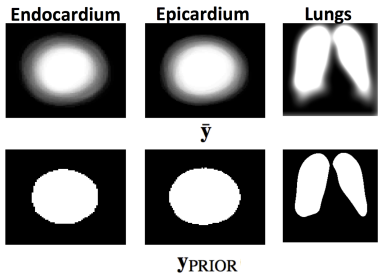


**Fig. 4** Shape priors $\mathbf{y}_{\text{PRIOR}}$ (computed from $\bar{\mathbf{y}}$ using (9)) for endocardium, epicardium and lungs.

The segmentation using the combination of DRLS, DBN and shape prior is explained in Alg. 1, which iteratively runs DRLS until convergence using the segmentation results from the DBN and from the shape prior as two of its optimisation terms. Notice that the initial segmentation $\phi_0$ can be manually provided, which results in a semi-automated segmentation, or automatically produced, generating a fully automated segmentation method.

**Algorithm 1** Combined DRLS and DBN Segmentation

1: INPUT: test image $\mathbf{v}$, shape prior $\mathbf{y}_{\text{PRIOR}}$ and initial segmentation $\phi_0$
2: Compute signed distance function $\phi_{\text{PRIOR}}$ from map $\mathbf{y}_{\text{PRIOR}}$ with (2)
3: Infer $\mathbf{y}_{\text{DBN}}$ from $\mathbf{v}$ using (5)
4: Compute signed distance function $\phi_{\text{DBN}}$ from map $\mathbf{y}_{\text{DBN}}$ with (2)
5: **for** t = 1:T **do**
6: Run DRLS using $\phi_{t-1}, \phi_{\text{DBN}}, \phi_{\text{PRIOR}}$ to produce $\phi_t$
7: **end for**
8: Segmentation is the zero level set $\mathscr{C} = \{\mathbf{x} \in \Omega | \phi_T(\mathbf{x}) = 0\}$

## *3.1 Left Ventricle Segmentation*

In this section, we present our **fully automated left ventricle segmentation method**. A cardiac cine MR sequence consists of $K$ volumes $\{\mathbf{V}_i\}_{i=1}^{K}$, each representing a particular cardiac phase, where each volume comprises a set of $N$ images $\{\mathbf{v}_j\}_{j=1}^{N}$, also known as volume slices, obtained using the short axis view (Fig. 5). We assume to have annotation only at the end diastolic (ED) and end systolic (ES) cardiac phases (i.e., only two out of the $K$ phases available) for all $N$ images in these two volumes. In each of these annotated images, the explicit endocardial and epicardial contour representations are denoted by $\mathbf{c}_{\text{ENDO}}$ and $\mathbf{c}_{\text{EPI}}$, respectively, and the segmentation maps are denoted by $\mathbf{y}_{\text{ENDO}}$ and $\mathbf{y}_{\text{EPI}}$. The set of annotated sequences is represented by $\mathscr{D} = \{(\mathbf{v}, \mathbf{c}_{\text{ENDO}}, \mathbf{c}_{\text{EPI}}, \mathbf{y}_{\text{ENDO}}, \mathbf{y}_{\text{EPI}}, i, q)_s\}_{s\in\{1,\ldots,S\}, i\in\{1,\ldots,N_s\}, q\in\{\text{ED,ES}\}}$, where

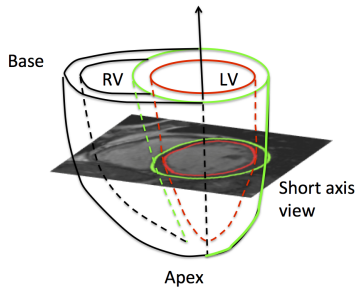


**Fig. 5** Visualisation of an image on the short axis view, where RV and LV stand for right and left ventricles, respectively, and the red contour represents the endocardium contour and green denotes the epicardium.

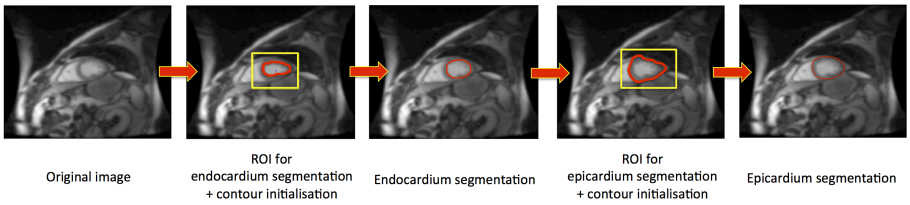


**Fig. 6** All steps for the left ventricle segmentation - Fig. 7 depicts each step in more detail.

$s$ denotes the sequence index (each sequence represents one patient), $i$ denotes the index to an image within the sequence $s$, and $q$ represents the cardiac phase (Fig. 2). Note that our methodology runs the segmentation process slice by slice in each of the ED and ES volumes, using the steps displayed in Fig. 6.

## *3.2 Endocardium Segmentation*

For segmenting the endocardium, it is first necessary to detect a region of interest (ROI) that fully contains the left ventricle. This ROI detection uses the structured inference computed from a DBN, which outputs an image region that is used in the estimation of the initial endocardium segmentation $\phi_0$ (see Alg. 1 and Fig. 7-(a)). The endocardium segmentation follows Alg. 1 and is represented in Fig. 7-(b). We explain the details of the endocardial segmentation below.

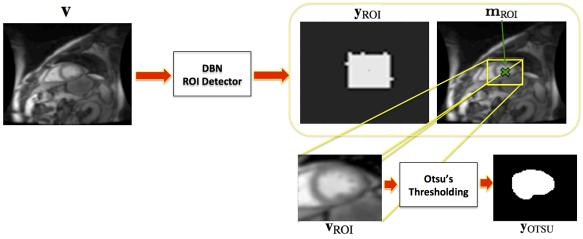


(a) ROI Detection and Initial Endocardium Segmentation

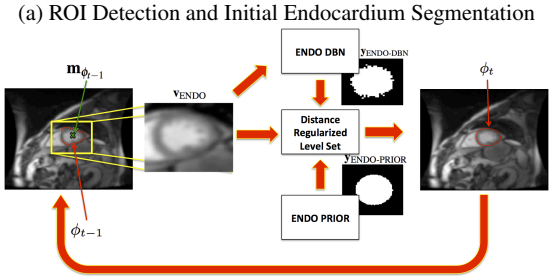


(b) Endocardium Segmentation

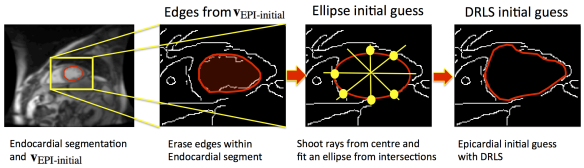


(c) Initial Epicardium Segmentation

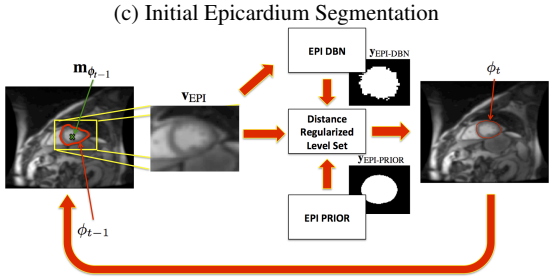


(d) Epicardium Segmentation

**Fig. 7** Models of the ROI detection and initial endocardium segmentation (a), final endocardium segmentation (b), initial epicardium segmentation (c) and final epicardium segmentation (d).

### 3.2.1 ROI DBN Detection and Initial Endocardium Segmentation

For the ROI detection, we use the DBN model introduced in (5), with parameters $\Theta_{\text{ROI}}$, that produces the segmentation map $\mathbf{y}_{\text{ROI}} : \Omega \rightarrow [0,1]$. The training set comprises images $\mathbf{v}$ and their respective ROI segmentation maps that are automatically built from the manual endocardial border delineations $\mathbf{c}_{\text{ENDO}}$ by producing a segmentation map with 0's everywhere except at a square of 1's with size $M_{\text{ROI}} \times M_{\text{ROI}}$,

centred at the centre of gravity of the annotation $\mathbf{c}_{\text{ENDO}}$ (see training samples in Fig. 8-(b)).

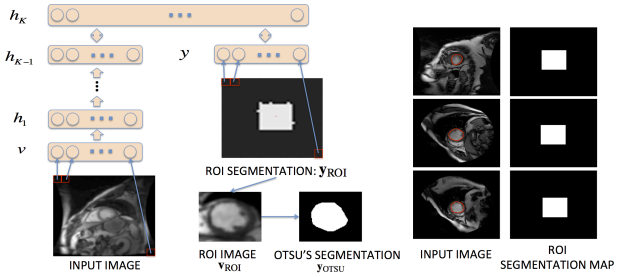


(a) ROI DBN & Otsu's segmentation (b) Training samples

**Fig. 8** ROI DBN Model and Otsu's segmentation (a) and training samples for the ROI DBN (b).

After estimating the ROI segmentation map $\mathbf{y}_{\text{ROI}}$, a rough endocardial border delineation is estimated by first applying the following function:

$$(\mathbf{v}_{\text{ROI}}, \mathbf{m}_{\text{ROI}}) = f_R(\mathbf{y}_{\text{ROI}}, \mathbf{v}, M_{\text{ROI}}), \tag{10}$$

where $\mathbf{m}_{\text{ROI}}$ is the centre of gravity of $\mathbf{y}_{\text{ROI}}$ computed as $\mathbf{m}_{\text{ROI}} = \int_\Omega \mathbf{x} h(\mathbf{y}_{\text{ROI}}) d\mathbf{x}$, with $h(\mathbf{y}_{\text{ROI}}) = \frac{H(\mathbf{y}^*_{\text{ROI}})}{\int_\Omega H(\mathbf{y}^*_{\text{ROI}}) d\mathbf{x}}$ and $H(.)$ denoting the Heaviside step function, and $\mathbf{v}_{\text{ROI}}$ is a sub-image of size $M_{\text{ROI}} \times M_{\text{ROI}}$ extracted with $\mathbf{v}_{\text{ROI}} = \mathbf{v}(\mathbf{m}_{\text{ROI}} \pm M_{\text{ROI}}/2)$. Then, Otsu's thresholding [34] is run on the sub-image $\mathbf{v}_{\text{ROI}}$, where the convex hull of the connected component linked to the centre $M_{\text{ROI}}/2$ is returned as the rough endocardial border delineation with $\mathbf{y}_{\text{OTSU}} = f_O(\mathbf{v}_{\text{ROI}})$, as displayed in Fig. 8-(a). Recall that Otsu's thresholding [34] is a segmentation method that binarizes a gray-level image using a threshold estimated to minimise the intra-class variance of the grey values, where the classes are defined by the pixel values above and below this threshold. This segmentation is used to form the initial signed distance function (Alg. 1), as follows:

$$\phi_0 = f_\phi(\mathbf{y}_{\text{OTSU}}, \mathbf{m}_{\text{ROI}}, M_{\text{ROI}}, \mathbf{v}), \tag{11}$$

where we first create a temporary binary map $\widehat{\mathbf{y}} : \Omega \to \{0,1\}$ with a map of the size of $\mathbf{v}$ containing only zeros, as in $\widehat{\mathbf{y}} = \mathbf{0}_{size(\mathbf{v})}$ (the function $size(i)$ returns the size of the image), then we fill this map with the result from $\mathbf{y}_{\text{OTSU}}$ centred at $\mathbf{m}_{\text{ROI}}$, with $\widehat{\mathbf{y}}(\mathbf{m}_{\text{ROI}} \pm M_{\text{ROI}}/2) = \mathbf{y}_{\text{OTSU}}(M_{\text{ROI}}/2 \pm M_{\text{ROI}}/2)$. Finally, the signed distance function $\phi_0$ is computed from $\widehat{\mathbf{y}}$ with (2).

### 3.2.2 Endocardium Segmentation Combining DRLS and DBN

Given the initial segmentation $\phi_0$ defined in (11), we run a slightly modified version of the segmentation method in Alg. 1. The main difference is the introduction of

an outer loop between lines 3 and 7, inclusive, which changes the sub-image of $\mathbf{v}$ that will be used as the input for the ENDO DBN, where the change is related to the sub-image centre given by the centre of gravity of $\phi_{t-1}$, computed with $\mathbf{m}_{\phi_{t-1}} = \int_{\Omega} \mathbf{x} h(\phi_{t-1}(\mathbf{x}))d\mathbf{x}$ with $h(\phi_{t-1}) = \frac{H(-\phi_{t-1})}{\int_{\Omega} H(-\phi_{t-1})d\mathbf{x}}$ (see Fig. 7-(b)). Also the segmentation in line 6 of Alg. 1 has inputs $\phi_{t-1}$, $\phi_{\text{ENDO-DBN},q}$ and $\phi_{\text{ENDO-PRIOR},q}$ (below, we provide details on these last two functions), with $t \in \{1,2,...,T\}$ and $q \in \{\text{ED,ES}\}$, where the shape terms, from (3), are denoted by $\mathscr{S}(\phi,\phi_{\kappa}) = \int_{\Omega}(\phi(\mathbf{x}) - \phi_{\kappa}(\mathbf{x} + \mathbf{m}_{\phi_{t-1}}))^2 d\mathbf{x}$ (with $\kappa \in \{(\text{ENDO-DBN},q),(\text{ENDO-PRIOR},q)\}$, and $q \in \{\text{ED,ES}\}$). This segmentation algorithm results in the signed distance function $\phi^*_{\text{ENDO},q}$, from which we can compute the estimated endocardial contour from its zero level set $\{\mathbf{x} \in \Omega | \phi^*_{\text{ENDO},q}(\mathbf{x}) = 0\}$ and endocardial binary segmentation map $\mathbf{y}^*_{\text{ENDO},q} = H(-\phi^*_{\text{ENDO},q})$.

The ENDO DBN used at this stage is the same as the one depicted in Fig. 3-(a), where the input image is a sub-image of $\mathbf{v}$ of size $M_{\text{ENDO}} \times M_{\text{ENDO}}$ centred at position $\mathbf{m}_{\phi_{t-1}}$, where this sub-image is represented by $\mathbf{v}_{\text{ENDO}}$. We have two distinct DBNs, one to segment images for $q = \text{ES}$ phase and another for $q = \text{ED}$ phase of the cardiac cycle, where the training set is formed by samples $\{(\mathbf{v}_{\text{ENDO}}, \mathbf{y}_{\text{ENDO}}, i, q)_s\}_{s\in\{1,...,S\},i\in\{1,...,N_s\},q\in\{\text{ED,ES}\}}$ extracted from the original training set with $f_R(.)$, defined in (10). The segmentation from ENDO DBN produces $\mathbf{y}_{\text{ENDO-DBN},q}$ from input $\mathbf{v}_{\text{ENDO}}$ using (5). The segmentation $\mathbf{y}_{\text{ENDO-DBN},q}$ can then be used to compute the signed distance function $\phi_{\text{ENDO-DBN},q}$ with (2). Finally, the ENDO shape prior, represented by $\mathbf{y}_{\text{ENDO-PRIOR},q}$, is computed as defined in (9) using the binary segmentation maps $\{(\mathbf{y}_{\text{ENDO}}, i, q)_s\}_{s\in\{1,...,S\},i\in\{1,...,N_s\},q\in\{\text{ED,ES}\}}$. Similarly, $\mathbf{y}_{\text{ENDO-PRIOR},q}$ is used to calculate the signed distance function $\phi_{\text{ENDO-PRIOR},q}$ with (2).

## *3.3 Epicardium Segmentation*

The epicardium segmentation also follows two steps, comprising an initial segmentation, which produces a square region containing the epicardium and an initial estimation of its border, similarly to the approach in Sec. 3.2.1 (Fig. 7-(c)). The second step involves an optimisation with DRLS [14], similar to the one presented above in Sec. 3.2.2 (Fig. 7-(d)).

### 3.3.1 Initial Epicardium Segmentation

The epicardium segmentation process is initialised with a rough delineation based on the endocardium detection (see Figure 7-(c)). Specifically, after the endocardium segmentation is finalized, we estimate the borders of the epicardium segmentation by first running the Canny edge detector [35] that outputs the edges within the sub-image $\mathbf{v}_{\text{EPI-initial}}$ of size $M_{\text{EPI}} \times M_{\text{EPI}}$ centred at position $\mathbf{m}_{\text{EPI-initial},q} =$

$\int_\Omega \mathbf{x} h(\phi^*_{\text{ENDO},q}(\mathbf{x}))d\mathbf{x}$ with $h(\phi^*_{\text{ENDO},q}) = \frac{H(-\phi^*_{\text{ENDO},q})}{\int_\Omega H(-\phi^*_{\text{ENDO},q})d\mathbf{x}}$. The edges lying in the region where $H(-\phi^*_{\text{ENDO},q})$ equals to one (this region represents blood pool found by the endocardium segmentation) are erased and then, by "shooting" 20 rays (18 degrees apart from each other) from the centre $\mathbf{m}_{\text{EPI-initial},q}$ and recording the intersection position between each ray and the first edge it crosses, we form a set of points that are likely to belong to the endocardial border. At this stage, since it is expected that the endocardial border will be relatively close to the epicardial border, we only record the points that are within a limited range from the original endocardial border (specifically, we expect the epicardial border to be within 1.05 and 1.1 of the length of the ray from $\mathbf{m}_{\text{EPI-initial}}$ to the endocardial border; otherwise no point is recorded - these numbers are estimated from the 95% confidence interval of the distance between the endocardium and epicardium annotations from the training set). Finally, by fitting an ellipse to these points and running a small number of iterations of the original DRLS [14] (which is the model in (1)-(3) with $\beta = \gamma = 0$), we form the initial epicardium segmentation that is represented by a map $\mathbf{y}_{\text{EPI-initial}}$, which is then used to form the initial signed distance function $\phi_0 = f_\phi(\mathbf{y}_{\text{EPI-initial}}, \mathbf{m}_{\text{EPI-initial}}, M_{\text{EPI}}, \mathbf{v})$, as defined in (2).

### 3.3.2 Epicardium Segmentation Combining DRLS and DBN

Using the initial epicardium segmentation $\phi_0$ from Sec. 3.3.1 above, we run the segmentation method in Alg. 1 with the same modification explained in Sec. 3.2.2 (i.e., the outer loop between lines 3 and 7 that changes the sub-image of $\mathbf{v}$ used in the input for the EPI DBN according to the centre of gravity $\mathbf{m}_{\phi_{t-1}}$ of $\phi_{t-1}$). The segmentation in line 6 of Alg. 1 has inputs $\phi_{t-1}$, $\phi_{\text{EPI-DBN},q}$ and $\phi_{\text{EPI-PRIOR},q}$ (please see details below on these last two functions), with $t \in \{1,2,...,T\}$ and $q \in \{\text{ED,ES}\}$, where the shape terms, from (3), are denoted by $\mathscr{S}(\phi,\phi_\kappa) = \int_\Omega (\phi(\mathbf{x}) - \phi_\kappa(\mathbf{x}+\mathbf{m}_{\phi_{t-1}}))^2 d\mathbf{x}$ (with $\kappa \in \{(\text{EPI-DBN},q),(\text{EPI-PRIOR},q)\}$, and $q \in \{\text{ED,ES}\}$). This segmentation algorithm results in the signed distance function $\phi^*_{\text{EPI},q}$, from which we can compute the estimated epicardial contour from its zero level set $\{\mathbf{x} \in \Omega | \phi^*_{\text{EPI},q}(\mathbf{x}) = 0\}$ and epicardial binary segmentation map $\mathbf{y}^*_{\text{EPI},q} = H(-\phi^*_{\text{EPI},q})$.

The EPI DBN is the same as the one displayed in Fig. 3-(a), where the input image is represented by $\mathbf{v}_{\text{EPI}}$, centred at $\mathbf{m}_{\phi_{t-1}}$ and of size $M_{\text{EPI}} \times M_{\text{EPI}}$. We can estimate the parameters of two DBNs for $q \in \{\text{ED,ES}\}$ with the following training set $\{(\mathbf{v}_{\text{EPI}}, \mathbf{y}_{\text{EPI}}, i, q)_s\}_{s\in\{1,...,S\},i\in\{1,...,N_s\},q\in\{ED,ES\}}$ extracted from the original training set with $f_R(.)$, defined in (10). The inference process is the same as the one defined in (5), resulting in $\mathbf{y}_{\text{EPI-DBN},q}$, which is used to compute the signed distance function $\phi_{\text{EPI-DBN},q}$ with (2). Finally, the EPI shape prior, denoted by $\mathbf{y}_{\text{EPI-PRIOR},q}$, is computed from (9) using the binary segmentation maps $\{(\mathbf{y}_{\text{EPI}}, i, q)_s\}_{s\in\{1,...,S\},i\in\{1,...,N_s\},q\in\{\text{ED,ES}\}}$. Similarly, $\mathbf{y}_{\text{EPI-PRIOR},q}$ is used to calculate the signed distance function $\phi_{\text{EPI-PRIOR},q}$ with (2).

### 3.4 Lung Segmentation

In this section, we present our **semi-automated lung segmentation method**. The annotated chest radiograph database (Fig. 2) is represented by $\mathscr{D} = \{(\mathbf{v}, \mathbf{c}, \mathbf{y}, q)_i\}_{i=1}^{|\mathscr{D}|}$, where $\mathbf{v}$ represents an image, $\mathbf{c}$ denotes the explicit contour representation, $\mathbf{y}$ the respective binary segmentation map, and $q \in \{\text{left lung,right lung}\}$.

The segmentation Algorithm 1 takes a manually provided initial segmentation $\phi_0$ and, in each iteration, uses the functions $\phi_{t-1}$, $\phi_{\text{DBN},q}$ and $\phi_{\text{PRIOR},q}$, with $t \in \{1,2,...,T\}$ and $q \in \{\text{left lung,right lung}\}$, and the final steady solution of this optimisation is represented by $\phi_q^*$, from which we can compute the estimated contour from the zero level set $\{\mathbf{x} \in \Omega | \phi_q^*(\mathbf{x}) = 0\}$ and the binary segmentation map $\mathbf{y}_q^* = H(-\phi_q^*)$. The DBN is the one shown in Fig. 3-(b), where the resulting segmentation $\mathbf{y}_{\text{DBN}}$ of both lungs is divided into two separate signed distance functions: $\phi_{\text{DBN,right lung}}$ for the right lung and $\phi_{\text{DBN,left lung}}$ for the left lung, where this separation is done via connected component analysis.

## 4 Experiments

### 4.1 Data Sets and Evaluation Measures

The proposed **endocardium and epicardium segmentation** method is assessed with the dataset and the evaluation introduced in the MICCAI 2009 LV segmentation challenge [4]. This dataset contains 45 cardiac short axis (SAX) cine-MR, which are divided into three sets (online, testing and training sets) of 15 sequences, with each sequence containing four ischemic heart failures, four non-ischemic heart failures, four LV hypertrophies and three normal cases. Each of those sequences has been acquired during a 10-15 second breath-holds, with a temporal resolution of 20 cardiac phases over the heart cycle, starting from the ED cardiac phase, and containing six to 12 SAX images obtained from the atrioventricular ring to the apex (thickness=8$mm$, gap=8$mm$, FOV=320$mm \times 320mm$, matrix= $256 \times 256$). Expert annotations are provided for endocardial contours in all slices at ED and ES cardiac phases, and for epicardial contours only at ED cardiac phase. The evaluation used to assess the algorithms submitted to the MICCAI 2009 LV segmentation challenge is based on the following three measures: 1) percentage of "good" contours, 2) the average Dice metric (ADM) of the "good" contours, and 3) average perpendicular distance (APD) of the "good" contours. A segmentation is classified as good if APD $< 5mm$. During the MICCAI 2009 LV Segmentation Challenge [4], the organisers first released the training and test sets, where the training set contained the manual annotation, but the test set did not include the manual annotation. The online dataset only became available a few days before the challenge day, so that the participants could submit their segmentation results for assessment. The challenge organisers reported all segmentation results for all datasets that were available from the par-

ticipants. Currently all three data sets with their respective expert annotations are publicly available. Given that most of the results from the challenge participants are available for the training and test sets, we decided to use the training set to estimate all DBN parameters, the online set for validating some DBN parameters (e.g., number of layers and number of nodes per layer), and the test set exclusively for testing (since this is the set which has the majority of results from the participants).

The proposed **lung segmentation** method is assessed with the Japanese Society of Radiological Technology (JSRT) dataset [16], which contains 247 chest radiographs with manual segmentations of lung fields, heart and clavicles [25]. Out of these 247 chest radiographs, 154 contain lung nodules (100 malignant, 54 benign) and 93 have no nodules, and each sample is represented by 12-bit gray scale image with size $2048 \times 2048$ pixels and $0.175mm$ pixel resolution. This database is randomly split into three sets: training (84 images), validation (40 images), and test (123 images), and the assessment is based on following three measures: Jaccard Similarity Coefficient ($\Omega$), Dice Coefficient (DSC), and Average Contour Distance (ACD) [5].

## *4.2 Experimental Setup*

For the **endocardium and epicardium segmentation**, the training set is used to model the ROI DBN, ENDO DBN and EPI DBN network (weights and biases), the shape priors and for estimating the weights of the DRLS method (i.e., $\mu, \lambda, \alpha, \beta, \gamma$ in (1) and (3)); while the online set is used for the model selection of the DBNs (i.e., the estimation of the number of hidden layers and the number of nodes per layer for the DBNs). For this model selection, we use the online set to estimate the number of hidden layers (from two to four hidden layers), and the number of nodes per hidden layer (from 100 to 2000 nodes per layer in intervals of 100 nodes). For the ROI DBN, the estimated model is as follows: 2 hidden layers with 1300 nodes in the first layer and 1500 in the second, and the input and segmentation layers with $40 \times 40$ nodes (i.e., the image is resized from $256 \times 256$ to $40 \times 40$ using standard blurring and downsampling techniques). For the ENDO DBN trained for the ED cycle, we reach the following model: 2 hidden layers with 1000 nodes in the first layer and 1000 in the second, and the input and segmentation layers with size $40 \times 40$ nodes (again, image is resized from $M_{\text{ENDO}} \times M_{\text{ENDO}}$ to $40 \times 40$). The ENDO DBN for the ES cycle has the following configuration: 2 hidden layers with 700 nodes in the first layer and 1000 in the second, and the input and segmentation layers with size $40 \times 40$. The EPI DBN for the ED cycle has the following configuration: 2 hidden layers with 1000 nodes in the first layer and 1000 in the second, and the input and segmentation layers with size $40 \times 40$ nodes (image resized from $M_{\text{EPI}} \times M_{\text{EPI}}$ to $40 \times 40$). For training all DBN models, we augment he training set, where we generate additional training images by translating the original training image (and its annotation) within a range of $\pm 10$ pixels. More specifically, we have 105 ED images and 75 ES annotated training images (from the 15 training volumes), and in

addition to the original training image, we generate 40 additional images with the translations mentioned above. Therefore, in total we have 105x41=4305 annotated images for training the ED endocardial DBN and epicardial DBN, and 75x41=3075 annotated images for training the ES endocardial DBN. The segmentation accuracy on training saturates with this augmented training data (i.e., adding more translated training images no longer improves the training results). The level set weights in (1) estimated with the training set for the endocardium segmentation are $\Delta t = 2$ (time step in the level set formulation), $\mu = \frac{0.24}{\Delta t} = 0.12, \lambda = 4, \alpha = -2, \beta = 0.02$, and $\gamma = 0.001$; and for the epicardium segmentation, we have $\Delta t = 2, \mu = \frac{0.24}{\Delta t} = 0.12, \lambda = 4, \alpha = -4, \beta = 0.015$, and $\gamma = 0.001$. The size of the sub-windows are set as $M_{\text{ROI}}, M_{\text{ENDO}}, M_{\text{EPI}} = 100$ (note that we found that the segmentation results are stable if $M_{\text{ROI}}, M_{\text{ENDO}}, M_{\text{EPI}} \in [80, 120]$).

For the **lung segmentation**, we use the training set for estimating the DBN and DRLS parameters and the validation set for the DBN model selection (similarly as for the ROI, ENDO and EPI DBN detailed above). This model selection estimated the following configuration for the DBN: two hidden layers, where each hidden layer has 1000 nodes and the input and segmentation layers have 1600 nodes. The initial guess $\phi_0$ in Alg. 1 is manually produced, so we show how the performance of our approach is affected by initial guesses of different accuracies, which are generated by random perturbations from the manual annotation. We denote the different initial guesses by the index $k \in \{1, 2, 3\}$, where $k = 1$ indicates the highest precision and $k = 3$ means the lowest precision initial guess. The estimation of the level set parameters is performed separately for each type of initial guess, and we achieve the following result: $\Delta t = 2$, $\mu = \frac{0.24}{\Delta t} = 0.12, \lambda = 2, \alpha = -3, \beta = 0, \gamma = 0.0005$ for $k = 1$; $\mu = 0.12, \lambda = 2, \alpha = -10, \beta = 0, \gamma = 0.003$ for $k = 2$; and $\mu = 0.12, \lambda = 2, \alpha = -15, \beta = 0, \gamma = 0.007$ for $k = 3$.

Note that for the level set weights in (1), we follow the recommendation by Li et al. [14] in defining the values for $\Delta t$, and $\mu$ (the recommendations are $\Delta t > 1$ and $\mu < \frac{0.25}{\Delta t}$), and for the inference procedure, the number of level set (DRLS) iterations is $T = 10$ (note that the segmentation results are stable if $T \in [5, 20]$).

### *4.3 Results of Each Stage of the Proposed Methodology*

The role of each stage of the proposed **endocardium segmentation** is presented in Table 1. The "Initial endocardium segmentation" shows the result produced by the zero level set of $\phi_0$ in (11) (i.e., the result from the ROI detection, followed by the initial endocardium segmentation). The "ENDO DBN alone" displays the accuracy results of the endocardium segmentation produced by the ENDO DBN (Sec. 3.2.2) alone. The "Model without DBN/shape prior" represents the energy functional in (3) with $\beta = \gamma = 0$, which effectively represents our model without the influence of the ENDO PRIOR and the ENDO DBN. Similarly the "Model without DBN" denotes the case where the functional in (3) has $\beta = 0$ (i.e., with no influence from ENDO DBN) and the "Model without shape prior" has $\gamma = 0$ (no influence from

ENDO PRIOR). Finally, the "Proposed model" displays the result with all steps described in Sec. 3.2, and "Proposed model (semi)" represents our model using a manual initialisation instead of the automated initialisation described in Sec. 3.2.1. This manual initialisation consists of a circle, where the centre is the manual annotation centre of gravity and the radius is the minimum distance between the manual annotation and this centre. The proposed **epicardium segmentation** is assessed in Table 2, which shows the result of the "initial epicardium segmentation" explained in Sec. 3.3.1, and the result of the segmentation produced by the complete model described in Sec. 3.3.2 (labelled as "Proposed model"). We also show the result of the semi-automated epicardium segmentation with manual initialisation (defined in the same way as the manual initialisation above for the endocardium segmentation), labelled as "Proposed model (semi)". Note that we do not show all steps in Table 2 because the results are similar to the initial epicardium segmentation.

Table 3 shows the results of our proposed methodology for **lung segmentation** with the different types of initial guesses. In this table, we also show the results when $\gamma = 0$, which is denoted by "Model without DBN" (this shows the influence of the DBN in the proposed methodology); and we also show the results for the initial guess, represented by "Initial guess only".

**Table 1** Quantitative experiments on the MICCAI 2009 challenge database [4] showing the **influence of each step** of the proposed methodology for the **endocardium segmentation**. Each cell is formatted as "mean (standard deviation) [min value - max value]".

| Method | "Good" Percentage | Endocardium ADM | Endocardium APD |
|---|---|---|---|
| **Test set (15 sequences)** | | | |
| Proposed model (semi) | 100(0)[100 – 100] | 0.91(0.03)[0.83 – 0.95] | 1.79(0.36)[1.28 – 2.75] |
| Proposed model | 95.91(5.28)[84.62 – 100] | 0.88(0.03)[0.82 – 0.93] | 2.34(0.46)[1.62 – 3.24] |
| Model without shape prior | 95.71(6.96)[78.95 – 100] | 0.88(0.03)[0.83 – 0.93] | 2.34(0.45)[1.67 – 3.14] |
| Model without DBN | 85.89(18.00)[36.84 – 100] | 0.84(0.04)[0.77 – 0.92] | 2.77(0.58)[1.73 – 3.74] |
| Model without DBN/shape prior | 84.49(18.31)[36.84 – 100] | 0.84(0.04)[0.78 – 0.92] | 2.78(0.58)[1.72 – 3.81] |
| ENDO DBN alone | 18.31(19.46)[0 – 100] | 0.87(0.02)[0.84 – 0.89] | 3.81(0.64)[2.97 – 4.88] |
| Initial endocardium segmentation | 85.18(15.83)[47.37 – 100] | 0.85(0.04)[0.79 – 0.92] | 2.81(0.47)[2.07 – 3.58] |
| **Training set (15 sequences)** | | | |
| Proposed model (semi) | 100(0)[100 – 100] | 0.91(0.03)[0.85 – 0.95] | 1.63(0.40)[1.29 – 2.70] |
| Proposed model | 97.22(3.16)[91.67 – 100] | 0.88(0.05)[0.76 – 0.95] | 2.13(0.46)[1.27 – 2.73] |
| Model without shape prior | 97.42(4.63)[83.33 – 100] | 0.88(0.04)[0.76 – 0.95] | 2.14(0.43)[1.28 – 2.63] |
| Model without DBN | 89.42(11.83)[61.11 – 100] | 0.85(0.06)[0.71 – 0.93] | 2.61(0.66)[1.74 – 3.65] |
| Model without DBN/shape prior | 88.11(13.84)[50.00 – 100] | 0.84(0.06)[0.70 – 0.93] | 2.57(0.62)[1.72 – 3.53] |
| ENDO DBN alone | 48.09(38.42)[0 – 100] | 0.86(0.05)[0.73 – 0.90] | 3.23(0.44)[2.70 – 4.05] |
| Initial endocardium segmentation | 89.61(11.57)[55.56 – 100] | 0.85(0.06)[0.71 – 0.93] | 2.71(0.57)[1.78 – 3.49] |

**Table 2** Quantitative experiments on the MICCAI 2009 challenge database [4] compared different versions of the proposed methodology for the **epicardium segmentation**. Each cell is formatted as "mean (standard deviation) [min value - max value]".

| Method | "Good" Percentage | Epicardium ADM | Epicardium APD |
|---|---|---|---|
| **Test set (15 sequences)** | | | |
| Proposed model (semi) | 100(0)[100 – 100] | 0.94(0.01)[0.92 – 0.97] | 1.73(0.28)[1.16 – 2.17] |
| Proposed model | 94.65(6.18)[85.71 – 100] | 0.93(0.02)[0.88 – 0.96] | 2.08(0.60)[1.27 – 3.74] |
| Initial epicardium segmentation | 94.65(6.18)[85.71 – 100] | 0.93(0.02)[0.88 – 0.96] | 2.19(0.58)[1.32 – 3.68] |
| **Training set (15 sequences)** | | | |
| Proposed model (semi) | 100.00(0.00)[100 – 100] | 0.94(0.01)[0.91 – 0.96] | 1.64(0.34)[1.17 – 2.47] |
| Proposed model | 98.52(5.74)[77.78 – 100] | 0.93(0.02)[0.89 – 0.96] | 1.99(0.46)[1.35 – 3.13] |
| Initial epicardium segmentation | 96.83(6.92)[77.78 – 100 | 0.93(0.02)[0.89 – 0.95] | 1.99(0.40)[1.46 – 3.14] |

**Table 3** Quantitative experiments on the JSRT database [16] showing the performance of the proposed **lung segmentation** method as a function of the initial guess used, where each cell is formatted as "mean (standard deviation) [min value - max value]".

| Initial guess | Method | $\Omega$ | DSC | ACD |
|---|---|---|---|---|
| $k=1$ | Proposed model | 0.985(0.003)[0.972 – 0.991] | 0.992(0.002)[0.986 – 0.996] | 1.075(0.065)[0.825 – 1.267] |
| | Model without DBN | 0.984(0.003)[0.969 – 0.990] | 0.992(0.002)[0.984 – 0.995] | 1.376(0.221)[1.234 – 6.184] |
| | Initial guess only | 0.955(0.006)[0.919 – 0.968] | 0.977(0.003)[0.958 – 0.984] | 1.392(0.006)[1.372 – 1.404] |
| $k=2$ | Proposed model | 0.973(0.007)[0.944 – 0.985] | 0.986(0.004)[0.971 – 0.993] | 1.120(0.165)[0.628 – 1.916] |
| | Model without DBN | 0.946(0.007)[0.910 – 0.961] | 0.972(0.004)[0.953 – 0.980] | 2.408(0.232)[0.021 – 7.232] |
| | Initial guess only | 0.912(0.013)[0.844 – 0.935] | 0.954(0.007)[0.916 – 0.967] | 2.519(0.041)[2.369 – 2.621] |
| $k=3$ | Proposed model | 0.948(0.012)[0.893 – 0.970] | 0.973(0.006)[0.943 – 0.985] | 1.852(0.286)[1.120 – 3.708] |
| | Model without DBN | 0.866(0.018)[0.790 – 0.900] | 0.928(0.010)[0.883 – 0.947] | 4.695(0.276)[3.792 – 9.112] |
| | Initial guess only | 0.828(0.024)[0.712 – 0.873] | 0.906(0.014)[0.832 – 0.932] | 4.936(0.105)[4.391 – 5.200] |

## *4.4 Comparison with the State of the Art*

Tables 4 and 5 shows a comparison between our methodology (labelled "Proposed model") and the state of the art for the **endocardium segmentation** problem, while Tables 6 and 7 displays a similar comparison for the **epicardium segmentation** problem for different subsets of the MICCAI 2009 challenge databases [4]. Most of the approaches on that table are based on active contour models [22, 18, 36, 21, 17, 37], machine learning models [19, 23], or a combination of both models [38]. Furthermore, Tables 4-7 also show a semi-automated version of our method (labelled "Proposed model (semi)") using the same initial guess described above in Sec. 4.3. Fig. 4.4 shows a few **endocardium and epicardium segmentation** results produced by our approach for challenging cases, such as with images from apical and basal slice images and presenting papillary muscles and trabeculations.

Table 8 compares the results of our proposed **lung segmentation** method with the ones produced by the current state of the art on the JSRT database. The most competitive methods in that table [5, 25] are based on hybrid methods based on

**Table 4** Quantitative experiments on the **training and test sets** of the MICCAI 2009 challenge databases [4] comparing the performance of our proposed approach with the state of the art on the **endocardium segmentation problem**. Notice that the methods are classified into fully or semi-automated. The cell formatting is the same as in Tab. 1, but note that '?' means that the result is not available in the literature. The top performance for each measure and dataset is highlighted.

| Method | "Good" Percentage | Endocardium ADM | Endocardium APD |
|---|---|---|---|
| **Test set (15 sequences)** | | | |
| **Semi Automated** | | | |
| **Proposed model (semi)** | **100(0)[100 – 100]** | **0.91(0.03)[0.83 – 0.95]** | **1.79(0.36)[1.28 – 2.75]** |
| [31] | 96.58(9.58)[63.15 – 100] | 0.89(0.03)[0.83 – 0.93] | 2.22(0.46)[1.69 – 3.30] |
| [18] | ? | 0.89(0.04)[?–?] | 2.10(0.44)[?–?] |
| **Fully Automated** | | | |
| **Proposed model** | **95.91(5.28)[84.62 – 100]** | 0.88(0.03)[0.82 – 0.93] | 2.34(0.46)[1.62 – 3.24] |
| [21] | 94.33(9.93)[62.00 – 100] | 0.88(0.03)[0.84 – 0.94] | 2.44(0.62)[1.36 – 3.68] |
| [23] | 86.47(11.00)[68.4 – 100] | **0.89(0.03)[0.82 – 0.94]** | 2.29(0.57)[1.67 – 3.93] |
| [17] | 72.45(19.52)[42.11 – 100] | **0.89(0.03)[0.84 – 0.94]** | **2.07(0.61)[1.32 – 3.77]** |
| [37] | ? | 0.86(0.04)[?–?] | ? |
| [19] | ? | 0.81(?)[?–?] | ? |

| Training set (15 sequences) | | | |
|---|---|---|---|
| **Semi Automated** | | | |
| **Proposed model (semi)** | **100(0)[100 – 100]** | **0.91(0.03)[0.85 – 0.95]** | **1.63(0.40)[1.29 – 2.70]** |
| [31] | 98.45(3.11)[91.66 – 100] | 0.90(0.03)[0.84 – 0.94] | 1.96(0.35)[1.43 – 2.55] |
| [18] | ? | **0.90(0.04)**[?–?] | 2.03(0.34)[?–?] |
| **Fully Automated** | | | |
| **Proposed model** | **97.22(3.16)[91.67 – 100]** | **0.88(0.05)[0.76 – 0.95]** | 2.13(0.46)[1.27 – 2.73] |
| [21] | 96.93(7.59)[72 – 100] | **0.88(0.06)[0.75 – 0.95]** | **2.09(0.53)[1.35 – 3.23]** |

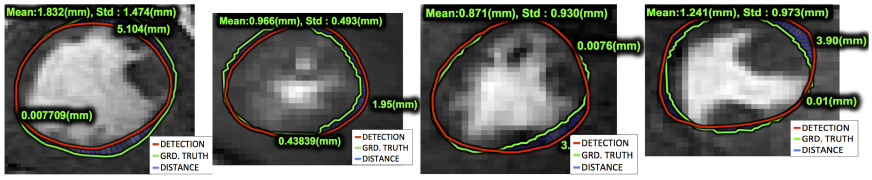


a) Results of endocardium segmentation on the test set

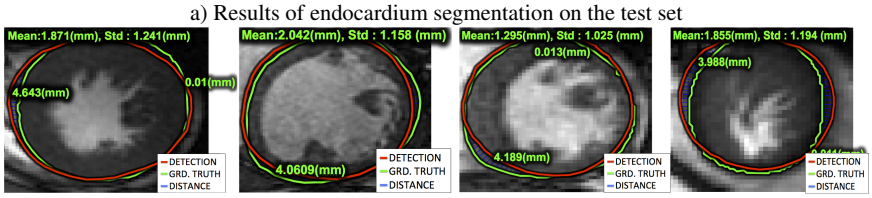


b) Results of epicardium segmentation on the test set

**Fig. 9** Epicardium and endocardium segmentation results with challenging cases, such as images from apical and basal slice images and presenting papillary muscles and trabeculations. The red contour denotes the automated detection, and green shows the manual annotation. For more results, please see the supplementary material.

**Table 5** Quantitative experiments on the **online and full sets** of the MICCAI 2009 challenge databases [4] comparing the performance of our proposed approach with the state of the art on the **endocardium segmentation problem**. Notice that the methods are classified into fully or semi-automated. The cell formatting is the same as in Tab. 1, but note that '?' means that the result is not available in the literature. The top performance for each measure and dataset is highlighted.

| Method | "Good" Percentage | Endocardium ADM | Endocardium APD |
|---|---|---|---|
| **Online set (15 sequences)** | | | |
| **Semi Automated** | | | |
| **Proposed model (semi)** | **100(0)[100 – 100]** | **0.91(0.03)[0.85 – 0.96]** | **1.78(0.49)[1.17 – 3.15]** |
| [31] | 98.71(3.66)[86.66 – 100] | 0.90(0.04)[0.83 – 0.95] | 2.04(0.35)[1.53 – 2.67] |
| **Fully Automated** | | | |
| **Proposed model** | **90.54(14.40)[46.67 – 100]** | **0.89(0.03)[0.82 – 0.94]** | **2.17(0.46)[1.62 – 3.46]** |

| | | | |
|---|---|---|---|
| **Full set (45 sequences)** | | | |
| **Semi Automated** | | | |
| **Proposed model (semi)** | **100(0)[100 – 100]** | **0.91(0.03)[0.83 – 0.96]** | **1.73(0.31)[1.17 – 3.15]** |
| [31] | 97.91(6.18)[63.15 – 100] | 0.90(0.03)[0.83 – 0.95] | 2.08(0.40)[1.43 – 3.30] |
| [22] | 91.00(8.00)[61 – 100] | 0.89(0.04)[0.80 – 0.96] | 1.94(0.42)[1.47 – 3.03] |
| **Fully Automated** | | | |
| **Proposed model** | **94.55(9.31)[46.67 – 100]** | 0.88(0.04)[0.76 – 0.95] | 2.22(0.46)[01.27 – 3.46] |
| [22] | 80.00(16.00)[29 – 100] | 0.86(0.05)[0.72 – 0.94] | 2.44(0.56)[1.31 – 4.20] |
| [38] | 91.06(9.42)[?–?] | **0.89(0.03)**[?–?] | 2.24(0.40)[?–?] |
| [36] | 79.20(19.00)[?–?] | **0.89(0.04)**[?–?] | **2.16(0.46)**[?–?] |

**Table 6** Quantitative experiments on the **training and test sets** of the MICCAI 2009 challenge databases [4] comparing the performance of our proposed approach with the state of the art on the **epicardium segmentation problem**. Notice that the methods are classified into fully or semi-automated. The cell formatting is the same as in Tab. 1, but note that '?' means that the result is not available in the literature. The top performance for each measure and dataset is highlighted.

| Method | "Good" Percentage | Epicardium ADM | Epicardium APD |
|---|---|---|---|
| **Test set (15 sequences)** | | | |
| **Semi Automated** | | | |
| **Proposed model (semi)** | **100(0)[100 – 100]** | **0.94(0.01)[0.92 – 0.97]** | **1.73(0.28)[1.16 – 2.17]** |
| [18] | ? | **0.94(0.01)**[?–?] | 1.95(0.34)[?–?] |
| **Fully Automated** | | | |
| **Proposed model** | 94.65(6.18)[85.71 – 100] | 0.93(0.02)[0.88 – 0.96] | 2.08(0.60)[1.27 – 3.74] |
| [21] | **95.60(6.90)[80.00 – 100]** | 0.93(0.02)[0.90 – 0.96] | 2.05(0.59)[1.28 – 3.29] |
| [23] | 94.20(7.00)[80.00 – 100] | 0.93(0.01)[0.90 – 0.96] | 2.28(0.39)[1.57 – 2.98] |
| [17] | 81.11(13.95)[57.14 – 100] | **0.94(0.02)[0.90 – 0.97]** | **1.91(0.63)[1.06 – 3.26]** |

| | | | |
|---|---|---|---|
| **Training set (15 sequences)** | | | |
| **Semi Automated** | | | |
| **Proposed model (semi)** | **100.00(0.00)[100 – 100]** | **0.94(0.01)[0.91 – 0.96]** | **1.64(0.34)[1.17 – 2.47]** |
| [18] | ? | 0.93(0.02)[?–?] | 2.28(0.42)[?–?] |
| **Fully Automated** | | | |
| **Proposed model** | 98.52(5.74)[77.78 – 100] | **0.93(0.02)[0.88 – 0.96]** | 1.99(0.46)[1.35 – 3.13] |
| [21] | **99.07(3.61)[86.00 – 100]** | **0.93(0.01)[0.91 – 0.95]** | **1.88(0.40)[1.20 – 2.55]** |

**Table 7** Quantitative experiments on the **online and full sets** of the MICCAI 2009 challenge databases [4] comparing the performance of our proposed approach with the state of the art on the **epicardium segmentation problem**. Notice that the methods are classified into fully or semi-automated. The cell formatting is the same as in Tab. 1, but note that '?' means that the result is not available in the literature. The top performance for each measure and dataset is highlighted.

| Method | "Good" Percentage | Epicardium ADM | Epicardium APD |
|---|---|---|---|
| **Online set (15 sequences)** | | | |
| **Semi Automated** | | | |
| **Proposed model (semi)** | **100.00(0.00)[100 – 100]** | **0.94(0.02)[0.88 – 0.96]** | **1.90(0.53)[1.22 – 3.16]** |
| **Fully Automated** | | | |
| **Proposed model** | **84.32(23.45)[12.50 – 100]** | **0.93(0.03)[0.84 – 0.95]** | **2.05(0.61)[1.39 – 3.63]** |

| | | | |
|---|---|---|---|
| **Full set (45 sequences)** | | | |
| **Semi Automated** | | | |
| **Proposed model (semi)** | **100(0)[100 – 100]** | **0.94(0.02)[0.88 – 0.97]** | **1.76(0.40)[1.16 – 3.16]** |
| [22] | 91.00(10.00)[70 – 100] | 0.92(0.02)[0.84 – 0.95] | 2.38(0.57)[1.28 – 3.79] |
| **Fully Automated** | | | |
| **Proposed model** | **92.49(15.31)[12.50 – 100]** | 0.93(0.02)[0.84 – 0.96] | **2.04(0.55)[1.27 – 3.70]** |
| [22] | 71.00(26.00)[0 – 100] | 0.91(0.03)[0.81 – 0.96] | 2.80(0.71)[1.37 – 4.88] |
| [38] | 91.21(8.52)[?–?] | **0.94(0.02)**[?–?] | 2.21(0.45)[?–?] |
| [36] | 83.90(16.80)[?–?] | 0.93(0.02)[?–?] | 2.22(0.43)[?–?] |

**Table 8** Quantitative experiments on the JSRT database [16] comparing our results with the state of the art on the same database, sorted from best (top) to worst (bottom). The symbol '?' indicates that the result is not available.

| Method | $\Omega$ | DSC | ACD |
|---|---|---|---|
| Proposed model, $k = 1$ | 0.985(0.003)[0.972 – 0.991] | 0.992(0.002)[0.986 – 0.996] | 1.075(0.065)[0.825 – 1.267] |
| Proposed model, $k = 2$ | 0.973(0.007)[0.944 – 0.985] | 0.986(0.004)[0.971 – 0.993] | 1.120(0.165)[0.628 – 1.916] |
| [5] | 0.954(0.015)[?–?] | 0.967(0.008)[?–?] | 1.321(0.316)[?–?] |
| [25] | 0.949(0.020)[0.818 – 0.978] | ?(?)[?–?] | 1.62(0.66)[0.95 – 7.72] |
| Proposed model, $k = 3$ | 0.948(0.012)[0.893 – 0.970] | 0.973(0.006)[0.943 – 0.985] | 1.852(0.286)[1.120 – 3.708] |
| [25] | 0.945(0.022)[0.823 – 0.972] | ?(?)[?–?] | 1.61(0.80)[0.83 – 8.34] |
| [39] | 0.940(0.053)[?–?] | ?(?)[?–?] | 2.46(2.06)[?–?] |
| [25] | 0.938(0.027)[0.823 – 0.968] | ?(?)[?–?] | 3.25(2.65)[0.93 – 15.59] |
| [25] | 0.934(0.037)[0.706 – 0.968] | ?(?)[?–?] | 2.08(1.40)[0.91 – 11.57] |
| [40] | 0.930(?)[?–?] | ?(?)[?–?] | ?(?)[?–?] |
| [25] | 0.922(0.029)[0.718 – 0.961] | ?(?))[?–?] | 2.39(1.07)[1.15 – 12.09] |
| [41] | 0.907(0.033)[?–?] | ?(?)[?–?] | ?(?)[?–?] |

MRF and appearance/shape active models. Finally, Fig. 4.4 shows a few lung segmentation results using initial guess $k = 2$ on images of the test set.

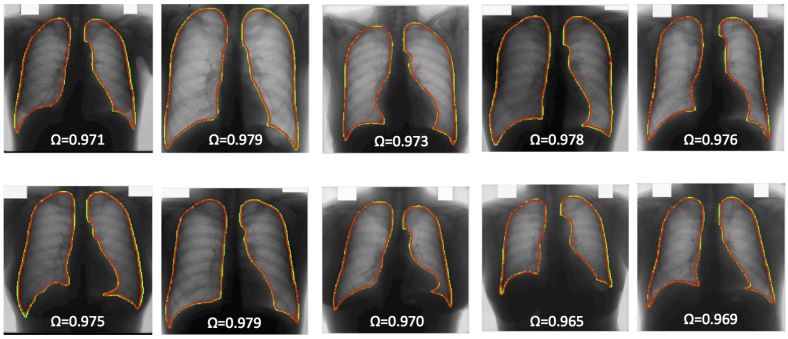


**Fig. 10** Lung segmentation results with initial guess $k = 2$. The green contour shows expert annotation and the red illustrates the final result.

## 5 Discussion and Conclusions

Table 1 clearly shows the importance of each stage of our proposed methodology for the endocardium segmentation problem. In particular, the initial endocardium segmentation is similar to the result from DRLS method [14] when the ENDO PRIOR and ENDO DBN terms are not used (row "Model without DBN/shape prior"). The introduction of shape prior (see row "Model without DBN") provides a slightly improvement to the initial segmentation, but it is not a significant change; therefore we could removed it from the framework in order to obtain small gains in terms of efficiency (if needed). The largest gain in terms of accuracy comes from the introduction of ENDO DBN (see row "Model without shape prior"), but note that ENDO DBN alone is not competitive, which implies that the results produced by ENDO DBN complements well the results from DRLS. The presence of all terms together, shows that our "Proposed model" produces better segmentation results than the DRLS and DBN methods. Also, notice the relative small differences between the training and testing segmentation results, which indicates good generalisation capabilities of our method (even with the relatively small training set of the MICCAI 2009 challenge database [4]). Finally, by using a manual initialisation, we obtain the best segmentation results in the field.

For the epicardium segmentation problem, Table 2 shows that the initial segmentation produces a result that is close to the final segmentation produced by our proposed model. This means that the EPI DBN provides a improvement that is not quite significant. Also note that the use of manual initialisation shows the best result in the field, similarly to the endocardium segmentation. Finally, one can question the need for two separate DBN models (i.e., ENDO and EPI DBNs) given their appearance similarities. The main reason for the use of these two models lies in the empirical evidence that they produce more accurate segmentation results, as shown in Tab. 4-5, where the rows labelled by **Proposed model (semi)** show the results

with the two separate DBNs, while the rows labelled by [31] display results using a single classifier.

The comparison with the state of the art for the problem of endocardium segmentation (Tables 4-5) and the epicardium segmentation (Tables 6-7) shows that the proposed approach has the best results for the semi-automated segmentation problem. When considering the fully automated segmentation, the results from the proposed method is comparable to the ones by [21], which is regarded as the current state of the art by a recent review paper by Petitjean et al. [3]. In regards to the "Good" percentage measure, our approach shows better results than the other methods; whilst in terms of ADM and ADP, our approach shows comparable results. When considering the epicardium segmentation, the results of our method are comparable to the one by Jolly's approach [21], but better than all others. It is important to note that although some approaches are more accurate in terms of APD or ADM [17], they also present low values for "Good" percentage, which means that these methods also produce a large number of segmentations with APD larger than 5*mm*, but the few ones that survive the "Good" percentage test are reasonably accurate. We also note the relatively worse performance of the fully automated approach compared to semi-automated segmentation (not only for our proposed method, but other methods in the literature), which implies that there is still an opportunity to improve further the accuracy of the initial endocardium and epicardium segmentations. In terms of running time, the system developed based on the proposed methodology runs on average in $175 \pm 35$ seconds for the endocardium segmentation and $119 \pm 20$ seconds for the epicardium segmentation using a *non-optimised Matlab program running on a standard computer* (Intel(R) Core(TM) i5-2500k 3.30GHz CPU with 8GB RAM), which is slower or comparable to other approaches that run between one minute [22, 21, 23] and three minutes [38, 17].

For the lung segmentation problem, Table 3 shows that the proposed model always improve over the initial guess, but this improvement is more obvious with poorer initial guesses (see results of "Initial guess only" and "Proposed mode" for $k = 3$). Another important observation is that the DRLS always improve over the initial guess, and the introduction of the DBN model improves the initial DRLS result. An obvious question is the reason for the absence of the shape prior model, and the reason is that we did not notice any empirical improvement. The comparison with the state of the art in Table 8 shows that with the manual initial guesses $k \in \{1,2\}$, our proposed approach produces the best results in the field. Additionally, using a similar Matlab code running on the same computer introduced above, our method runs on average in 20.68 seconds/image, which is comparable to the result by Candemir et al. [5], who report a running time of between 20 and 25 seconds/image using the same input resolution and similar computer configuration.

There are several points that can be explored in order to improve the results above. For the endocardium and epicardium segmentation, we can run the method over the whole volume and use a 3-D shape model to constrain the search process. We can also use a motion model to constrain the segmentation process. More complex DBN models can be trained when new training sets become available. Finally, we can decrease the running time of our approach by parallelising the segmentation

processes since the segmentation of each slice is done independently of all others (roughly this means that we can in principle make our approach 10 times faster). For the lung segmentation, we plan to introduce an automated initial guess with a method similar to the one proposed by Candemir et al. [5]. Furthermore, we plan to extend this method to other segmentation problems.

In this chapter we have presented a methodology that combines level set method and structured output deep belief network models. We show the functionality of the proposed approach in two different problems: the segmentation of endocardium and epicardium from cine MR and the segmentation of lungs from chest radiographs. In both problems we show extensive experiments that show the functionality of our approach, and they also show that our approach produces the current state-of-the-art segmentation results.

## Acknowledgements

This work was partially supported by the Australian Research Council's Discovery Projects funding scheme (project DP140102794). Tuan Anh Ngo acknowledges the support of the 322 Program - Vietnam International Education Development, Ministry of Education and Training (VIED-MOET).

## References

1. T. Ngo and G. Carneiro, "Fully automated non-rigid segmentation with distance regularized level set evolution initialized and constrained by deep-structured inference," in *Proceedings of the IEEE Conference on Computer Vision and Pattern Recognition*, 2014, pp. 3118–3125.
2. T. A. Ngo and G. Carneiro, "Lung segmentation in chest radiographs using distance regularized level set and deep-structured learning and inference," in *Image Processing (ICIP), 2015 IEEE International Conference on*. IEEE, 2015, pp. 2140–2143.
3. C. Petitjean and J.-N. Dacher, "A review of segmentation methods in short axis cardiac mr images," *Medical Image Analysis*, vol. 15, no. 2, pp. 169–184, 2011.
4. P. Radau, Y. Lu, K. Connelly, G. Paul, A. Dick, and G. Wright, "Evaluation framework for algorithms segmenting short axis cardiac mri," *MIDAS J.Cardiac MR Left Ventricle Segmentation Challenge*, 2009.
5. S. Candemir, S. Jaeger, J. Musco, Z. Xue, A. Karargyris, S. Antani, G. Thoma, and K. Palaniappan, "Lung segmentation in chest radiograps using anatomical atlases with non-rigid registration," 2014.
6. F. M. Carrascal, J. M. Carreira, M. Souto, P. G. Tahoces, L. Gómez, and J. J. Vidal, "Automatic calculation of total lung capacity from automatically traced lung boundaries in postero-anterior and lateral digital chest radiographs," *Medical physics*, vol. 25, no. 7, pp. 1118–1131, 1998.
7. M. Kass, A. Witkin, and D. Terzopoulos, "Snakes: Active contour models," *International journal of computer vision*, vol. 1, no. 4, pp. 321–331, 1988.
8. S. Osher and J. A. Sethian, "Fronts propagating with curvature-dependent speed: algorithms based on hamilton-jacobi formulations," *Journal of computational physics*, vol. 79, no. 1, pp. 12–49, 1988.

9. T. F. Cootes, C. J. Taylor, D. H. Cooper, and J. Graham, "Active shape models-their training and application," *Computer vision and image understanding*, vol. 61, no. 1, pp. 38–59, 1995.
10. B. Georgescu, X. S. Zhou, D. Comaniciu, and A. Gupta, "Databased-guided segmentation of anatomical structures with complex appearance," in *CVPR*, 2005.
11. D. Cobzas and M. Schmidt, "Increased discrimination in level set methods with embedded conditional random fields," in *Computer Vision and Pattern Recognition, 2009. CVPR 2009. IEEE Conference on*. IEEE, 2009, pp. 328–335.
12. R. Huang, V. Pavlovic, and D. N. Metaxas, "A graphical model framework for coupling mrfs and deformable models," in *Computer Vision and Pattern Recognition, 2004. CVPR 2004. Proceedings of the 2004 IEEE Computer Society Conference on*, vol. 2. IEEE, 2004, pp. II–739.
13. G. Tsechpenakis and D. N. Metaxas, "Crf-driven implicit deformable model," in *Computer Vision and Pattern Recognition, 2007. CVPR'07. IEEE Conference on*. IEEE, 2007, pp. 1–8.
14. C. Li, C. Xu, C. Gui, and M. D. Fox, "Distance regularized level set evolution and its application to image segmentation," *Image Processing, IEEE Transactions on*, vol. 19, no. 12, pp. 3243–3254, 2010.
15. G. Hinton and R. Salakhutdinov, "Reducing the dimensionality of data with neural networks," *Science*, vol. 313, no. 5786, pp. 504–507, 2006.
16. J. Shiraishi, S. Katsuragawa, J. Ikezoe, T. Matsumoto, T. Kobayashi, K.-i. Komatsu, M. Matsui, H. Fujita, Y. Kodera, and K. Doi, "Development of a digital image database for chest radiographs with and without a lung nodule: receiver operating characteristic analysis of radiologists' detection of pulmonary nodules," *American Journal of Roentgenology*, vol. 174, no. 1, pp. 71–74, 2000.
17. Y. Lu, P. Radau, K. Connelly, A. Dick, and G. Wright, "Automatic image-driven segmentation of left ventricle in cardiac cine mri," *The MIDAS Journal*, vol. 49, 2009.
18. S. Huang, J. Liu, L. Lee, S. Venkatesh, L. Teo, C. Au, and W. Nowinski, "Segmentation of the left ventricle from cine mr images using a comprehensive approach," *The MIDAS Journal*, vol. 49, 2009.
19. S. O'Brien, O. Ghita, and P. Whelan, "Segmenting the left ventricle in 3d using a coupled asm and a learned non-rigid spatial model," *The MIDAS Journal*, vol. 49, 2009.
20. J. Schaerer, C. Casta, J. Pousin, and P. Clarysse, "A dynamic elastic model for segmentation and tracking of the heart in mr image sequences," *Medical Image Analysis*, vol. 14, no. 6, pp. 738–749, 2010.
21. M. Jolly, "Fully automatic left ventricle segmentation in cardiac cine mr images using registration and minimum surfaces," *The MIDAS Journal*, vol. 49, 2009.
22. C. Constantinides, E. Roullot, M. Lefort, and F. Frouin, "Fully automated segmentation of the left ventricle applied to cine mr images: Description and results on a database of 45 subjects," in *Engineering in Medicine and Biology Society (EMBC), 2012 Annual International Conference of the IEEE*. IEEE, 2012, pp. 3207–3210.
23. J. Wijnhout, D. Hendriksen, H. Assen, and R. der Geest, "Lv challenge lkeb contribution: Fully automated myocardial contour detection," *The MIDAS Journal*, vol. 43, 2009.
24. B. Van Ginneken, A. F. Frangi, J. J. Staal, B. M. ter Haar Romeny, and M. A. Viergever, "Active shape model segmentation with optimal features," *medical Imaging, IEEE Transactions on*, vol. 21, no. 8, pp. 924–933, 2002.
25. B. Van Ginneken, M. B. Stegmann, and M. Loog, "Segmentation of anatomical structures in chest radiographs using supervised methods: a comparative study on a public database," *Medical Image Analysis*, vol. 10, no. 1, pp. 19–40, 2006.
26. G. BakIr, *Predicting structured data*. MIT press, 2007.
27. I. Tsochantaridis, T. Joachims, T. Hofmann, Y. Altun, and Y. Singer, "Large margin methods for structured and interdependent output variables." *Journal of Machine Learning Research*, vol. 6, no. 9, 2005.
28. M. Collins, "Discriminative training methods for hidden markov models: Theory and experiments with perceptron algorithms," in *Proceedings of the ACL-02 conference on Empirical methods in natural language processing-Volume 10*. Association for Computational Linguistics, 2002, pp. 1–8.

29. I. Fasel and J. Berry, "Deep belief networks for real-time extraction of tongue contours from ultrasound during speech," in *Pattern Recognition (ICPR), 2010 20th International Conference on*. IEEE, 2010, pp. 1493–1496.
30. C. Farabet, C. Couprie, L. Najman, and Y. LeCun, "Scene parsing with multiscale feature learning, purity trees, and optimal covers," *arXiv preprint arXiv:1202.2160*, 2012.
31. T. A. Ngo and G. Carneiro, "Left ventricle segmentation from cardiac mri combining level set methods with deep belief networks," in *Image Processing (ICIP), 2013 20th IEEE International Conference on*. IEEE, 2013, pp. 695–699.
32. ——, "Fully automated non-rigid segmentation with distance regularized level set evolution initialized and cosntrained by deep-structured inference," in *Computer Vision and Pattern Recognition (CVPR), 2013 IEEE Conference on*. IEEE, 2014.
33. D. Cremers, S. J. Osher, and S. Soatto, "Kernel density estimation and intrinsic alignment for shape priors in level set segmentation," *International Journal of Computer Vision*, vol. 69, no. 3, pp. 335–351, 2006.
34. N. Otsu, "A threshold selection method from gray-level histograms," *Automatica*, vol. 11, no. 285-296, pp. 23–27, 1975.
35. J. Canny, "A computational approach to edge detection," *Pattern Analysis and Machine Intelligence, IEEE Transactions on*, no. 6, pp. 679–698, 1986.
36. S. Huang, J. Liu, L. C. Lee, S. K. Venkatesh, L. L. San Teo, C. Au, and W. L. Nowinski, "An image-based comprehensive approach for automatic segmentation of left ventricle from cardiac short axis cine mr images," *Journal of digital imaging*, vol. 24, no. 4, pp. 598–608, 2011.
37. L. Marak, J. Cousty, L. Najman, H. Talbot *et al.*, "4d morphological segmentation and the miccai lv-segmentation grand challenge," in *MICCAI 2009 Workshop on Cardiac MR Left Ventricle Segmentation Challenge*, no. 1, 2009, pp. 1–8.
38. H. Hu, H. Liu, Z. Gao, and L. Huang, "Hybrid segmentation of left ventricle in cardiac mri using gaussian-mixture model and region restricted dynamic programming," *Magnetic resonance imaging*, 2012.
39. A. Dawoud, "Lung segmentation in chest radiographs by fusing shape information in iterative thresholding," *IET Computer Vision*, vol. 5, no. 3, pp. 185–190, 2011.
40. D. Seghers, D. Loeckx, F. Maes, D. Vandermeulen, and P. Suetens, "Minimal shape and intensity cost path segmentation," *Medical Imaging, IEEE Transactions on*, vol. 26, no. 8, pp. 1115–1129, 2007.
41. T. Yu, J. Luo, and N. Ahuja, "Shape regularized active contour using iterative global search and local optimization," in *Computer Vision and Pattern Recognition, 2005. CVPR 2005. IEEE Computer Society Conference on*, vol. 2. IEEE, 2005, pp. 655–662.